Infrared Physics & Technology 89 (2018) 194–202

Contents lists available at ScienceDirect

Infrared Physics & Technology

journal homepage: www.elsevier.com/locate/infrared

Regular article

A novel, highly efficient cavity backshort design for far-infrared TES detectors

C. Bracken [a,b,*], G. de Lange [c], M.D. Audley [c], N. Trappe [a], J.A. Murphy [a], M. Gradziel [a], W-J. Vreeling [c], D. Watson [a]

[a] Department of Experimental Physics, Maynooth University, Ireland
[b] Astronomy & Astrophysics Section, School of Cosmic Physics, Dublin Institute for Advanced Studies, 31 Fitzwilliam Place, Dublin 2, Ireland
[c] Netherlands Institute for Space Research (SRON), Groningen, The Netherlands

HIGHLIGHTS

- An improved cavity backshort coupling scheme for TES (transition edge sensors).
- Increased coupling of the incoming astronomical signal to the TES detectors.
- Improved cavity geometry, resulting from anisotropic silicon crystal etching process.
- Novel, efficient mode-matching code for modelling electrically large structures.

ARTICLE INFO

Article history:
Received 27 August 2017
Revised 3 January 2018
Accepted 5 January 2018
Available online 11 January 2018

Keywords:
Transition edge sensor
Far-infrared
Anisotropic silicon crystal etching
VNA
Cavity backshort
Bolometer
FTS

ABSTRACT

In this paper we present a new cavity backshort design for TES (transition edge sensor) detectors which will provide increased coupling of the incoming astronomical signal to the detectors. The increased coupling results from the improved geometry of the cavities, where the geometry is a consequence of the proposed chemical etching manufacturing technique. Using a number of modelling techniques, predicted results of the performance of the cavities for frequencies of 4.3–10 THz are presented and compared to more standard cavity designs. Excellent optical efficiency is demonstrated, with improved response flatness across the band. In order to verify the simulated results, a scaled model cavity was built for testing at the lower W-band frequencies (75–100 GHz) with a VNA system. Further testing of the scale model at THz frequencies was carried out using a globar and bolometer via an FTS measurement set-up. The experimental results are presented, and compared to the simulations. Although there is relatively poor comparison between simulation and measurement at some frequencies, the discrepancies are explained by means of higher-mode excitation in the measured cavity which are not accounted for in the single-mode simulations. To verify this assumption, a better behaved cylindrical cavity is simulated and measured, where excellent agreement is demonstrated in those results. It can be concluded that both the simulations and the supporting measurements give confidence that this novel cavity design will indeed provide much-improved optical coupling for TES detectors in the far-infrared/THz band.

© 2018 Elsevier B.V. All rights reserved.

1. Introduction

If future far-infrared space observatories such as the proposed SPICA mission [1,2] are to go beyond the sensitivity limits of their predecessors (e.g. HSO [3,4] and Spitzer [5]), detectors with extremely low intrinsic noise must be combined with an efficient optical coupling scheme. Ongoing work at the far-infrared TES detector test facility at SRON Groningen is pushing the sensitivity limits of far-infrared detectors at frequencies that will allow the THz gap to be truly bridged. The TES detectors being tested there are routinely showing NEP_{dark} of 2×10^{-18} W/$\sqrt{\text{Hz}}$ and saturation powers below 10 fW at wavelengths as short as $30 - 60$ μm [6]. In order to take advantage of these extremely high sensitivities it is important to employ an efficient optical coupling scheme. The cavity backshort format currently used in the SRON TES detector test facility is a hemisphere, as shown in Fig. 3 (left). The main

* Corresponding author at: Astronomy & Astrophysics Section, School of Cosmic Physics, Dublin Institute for Advanced Studies, 31 Fitzwilliam Place, Dublin 2, Ireland.
E-mail address: cbracken@cp.dias.ie (C. Bracken).
URL: https://www.dias.ie/2017/06/22/dr-colm-bracken (C. Bracken).

https://doi.org/10.1016/j.infrared.2018.01.004
1350-4495/© 2018 Elsevier B.V. All rights reserved.

reason for defaulting to this hemispherical geometry was due to its relative ease of manufacture through mechanical machining, and the geometrical assumption that placing the detector at the centre of the hemisphere would focus the signal onto it.

It has been shown previously however that there are indeed more optimum solutions such as a sinusoidally varying backshort wall [7]. However, creating these more complicated geometries to a high level of accuracy with mechanical machining becomes very difficult at the micron-scales required for the shortest wavelengths of the far-infrared band. Another backshort geometry that has been shown to provide improved coupling over that of the hemisphere is a pyramidal shape [8,7]. The benefit of choosing a pyramidal geometry over a sinusoid is that a pyramid can be chemically etched from a silicon wafer using a technique called anisotropic silicon crystal etching [9–11]. Using this chemical etching method on the appropriate crystal face naturally results in a pyramidal micro-cavity with an apex angle of 71°. Further improvement can been achieved if two such pyramid structures are employed in a back-to-back format, with the absorber layer and TES detector located where the two pyramids join (Fig. 3 (right)).

2. Cavity and backshort designs

2.1. Purpose of cavity and backshort

The purpose of a detector backshort, in front of which the TES and absorber layer are housed, is to help couple the astronomical signal to the thin absorbing layer of Ta. If the impedance of the Ta layer is matched to free-space (377 $\Omega\,Sq^{-1}$), approximately half of the radiation will be absorbed and half transmitted upon propagating across the Ta absorber. The part of the signal that is transmitted must then be reflected by the backshort, back toward the absorber, where again roughly half of the remaining signal will be absorbed.

A full cavity structure is intended to provide multiple reflections and thus multiple passes of the signal across the Ta absorber. The highly sensitive TES, which is coupled to the Ta absorber then detects the minute increase in temperature due to the signal absorbed by the Ta. Inevitably some level of signal will be returned back through the waveguide feed, and some will be lost through the free-space gap (if present) between the waveguide and cavity-backshort, as is the case with the current design used in the TES testbed [12]. The purpose of the free-space gap is to allow some distance between the delicate TES array chip and the metal block that contains the feed horn array, as vibrations during launch could cause damage if the two were to come into contact.

2.2. Current typical designs

The most commonly utilised backshort designs for the far-infrared wavebands are simple flat surfaces [13,14] as shown in Figs. 1 and 3 (centre), based on the quarter-wavelength resonance approach. However, given that the quarter wavelength backshort distance corresponds to one particular wavelength value within the design waveband (usually the central wavelength), such detector arrangements can often have poor coupling at wavelengths not close to the centre of the waveband. So, for a single propagating EM mode, each wavelength/frequency within a given band will have its own specific ideal backshort distance, and this is illustrated in Figs. 1 and 2 (left). The problem becomes more complicated when one considers an over-moded detector pixel. As well as the usual frequency dependence for the ideal backshort distance, each EM mode exhibits maximum coupling at a different backshort distance for a given frequency. This is illustrated in Fig. 2 (right), where the fractional power absorbed corresponds to the average absorption across the band. For instruments designed for wavebands spanning a full octave or more, this can clearly be an issue.

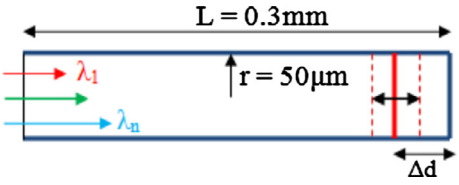

Fig. 1. A model of a cylindrical waveguide with radius $r = 50\,\mu m$. For the fundamental TE_{11} EM mode, propagating at a frequency of, say, $\nu = 5$ THz ($\lambda = 60\,\mu m$), the backshort distance will be $\Delta d = \lambda/4 = 15\,\mu m$.

2.3. Improved design

It was determined that the best approach to increasing the coupling of signal to the absorber, across a large waveband, was to find a more optimum geometry backshort to that of the hemisphere or flat backshort, while at the same time reducing or removing the free-space gap. Furthermore, a more precise manufacturing technique was desired as it is clearly difficult to machine smooth, profiled micro cavities using mechanical machining methods. The novel manufacturing technique of isotropic or anisotropic silicon crystal etching allows the fabrication of extremely smooth cavities with hemisphere or pyramidal geometries, respectively [10,11]. Further improvements in surface finish, with root mean square roughness values smaller than 20 nm can be achieved if the etching is carried out in an ultrasonic bath [15]. In general the chemical etching method results in a smoother, sharper, burr-free surface finish [16]. Although no analysis of the potential benefits of a smoother surface finish were carried out in this paper, the technique provides a means to easily achieving more complex geometries with improved coupling properties for the signal. Finally, if two such cavity structures could be used back-to-back then the free-space gap could be eliminated while still providing some distance between the TES and waveguide (see Fig. 3 (right)).

3. Computational models

3.1. Finite element model

In order to simulate the performance of the new pyramidal cavity design, a frequency domain FEM (finite element method) model was built using the RF module in the COMSOL Multiphysics package [17]. PEC and PMC boundary conditions were employed to reduce the size of the problem by a factor of 4, and the walls of the cavity were given PEC boundaries. The cavity was fed by a square waveguide with dimensions of 100 μm^2, and the Ta absorber was represented by an infinitely thin (geometrically) layer with sheet resistance of 377 Ω $square^{-1}$. It has previously been theoretically shown that this approximation holds true for a Ta layer with thickness $\delta \leqslant 10$ nm [18], and the actual thickness of the Ta currently used in the SAFARI pixel testbed is $\delta \approx 7$ nm. The waveguide was excited with a TE_{10} waveguide mode, where it was assumed that the horn and waveguide would be single-moded. In reality, given the dimensions of the waveguide, a number of higher-order modes will also be present at the higher frequencies, the number of which will depend on the field of view of the optics.

The fraction of power absorbed by the Ta sheet can either be determined indirectly by analysing the return power using (1) (since there are no other losses assumed) [19,20], or by performing a surface integral across the Ta layer using 2 [21]. The parameter to be integrated is the surface resistive heating which is a result of induced currents across the Ta. Both methods were used to

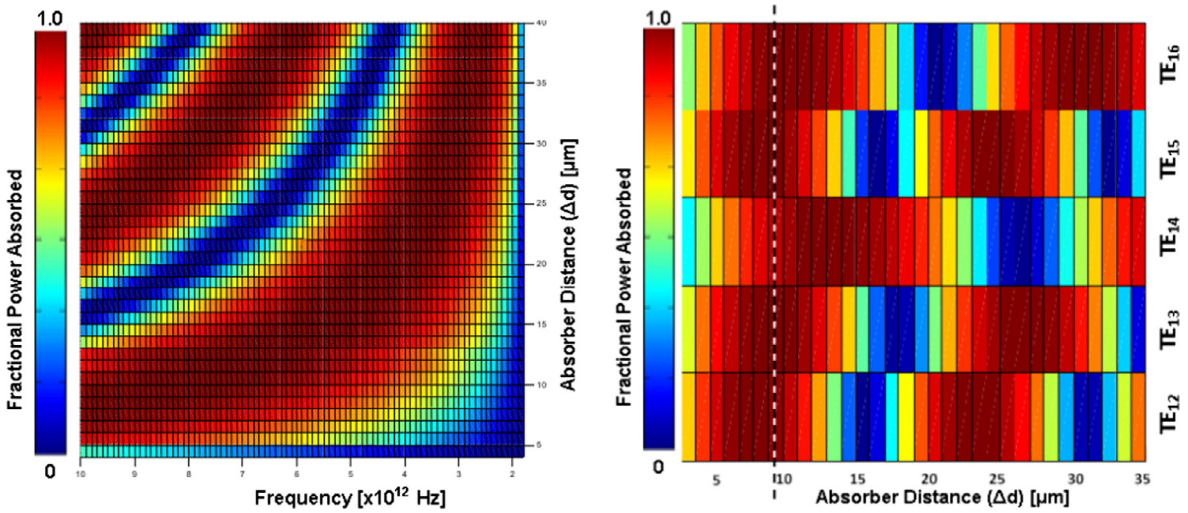

Fig. 2. *Left*: Coupling of signal to Ta absorber as a function of frequency and absorber-backshort distance. *Right*: Average coupling (across band) of signal to Ta absorber as a function of absorber-backshort distance and mode number.

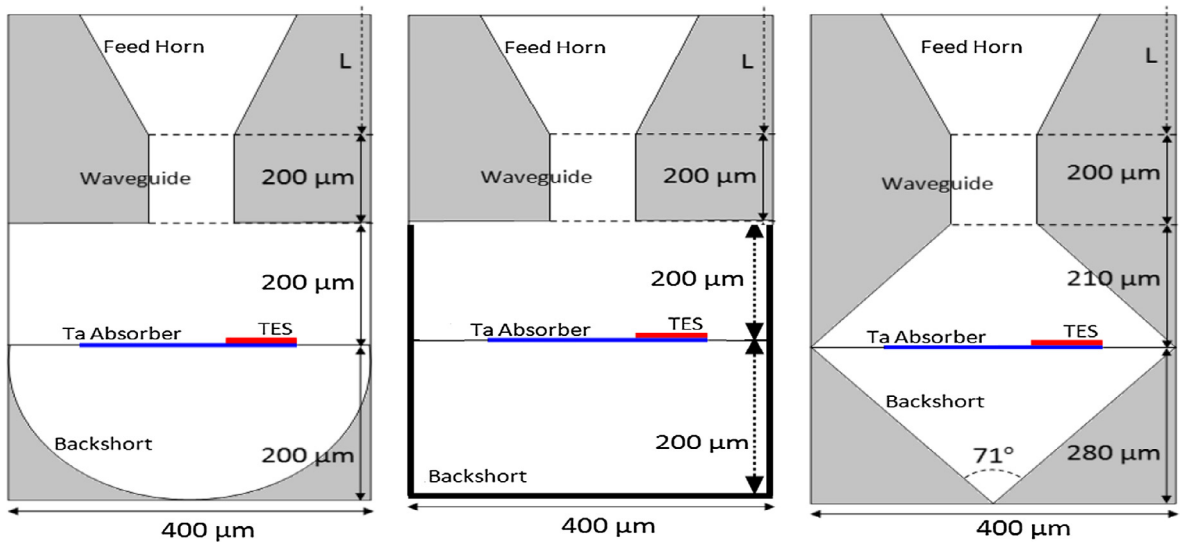

Fig. 3. *Left*: The cavity backshort format currently being used in the SAFARI pixel testbed. *Centre*: Another typical (flat) cavity backshort design often used. *Right*: The new cavity design concept that utilises the natural pyramidal shape that results from chemically etching a silicon wafer appropriately. The square waveguide has a cross-section of 100 μm^2 in each case.

calculate the predicted spectral 'efficiency' of various absorber sizes within the double-pyramid cavity structure, the results of which are shown in Figs. 5 and 6.

$$P'_{Abs} = 1 - S_{11}^2 \tag{1}$$

$$P_{Abs} = \int\int_S \frac{1}{2} Re\left(\vec{J_S} \cdot \vec{E}\right) \cdot dS \tag{2}$$

3.2. Mode-matching model

Due to the high computational memory demands when modelling high frequencies with the FEM approach, an alternative modelling technique was also employed. A novel EM mode-matching program was developed in-house [22], where the fields are formulated as a sum of TE (transverse electric) and TM (transverse magnetic) modes. The power transmitted through a system is analysed by calculating power coupling integrals at planes where there is discontinuity in the geometry, and ensuring power is conserved. Overall scattering matrices are constructed which represent either the modal power transmitted through the entire system ($\vec{S_{21}}$), or the return modal power ($\vec{S_{11}}$). The behaviour of the resistive absorber sheet can also be included by defining special boundary conditions for the integrals at the plane where the absorber is positioned [23,24]. An analysis of the total return power (which would be unity for an empty cavity, and less than unity if there is an absorber present) can then be used to deduce the amount of power absorbed by the Ta. The calculation is similar to that of Eq. (1), except that the S_{11} factor is replaced by a summation over the elements of the first row of the matrix $\vec{S_{11}}$, since those elements correspond to weighting factors for the reflected modes of the system. This mode-matching approach is very computationally efficient as it takes advantage of symmetry in terms of the modal solutions to the wave equation within square or rectangular geometries, as well as the analytical forms that can be found for the integrals.

The efficient mode-matching code provides an extremely fast analysis approach for simulating absorbers in electrically large structures. Using this method, a number of cavity backshort geometries were analysed across the highest frequencies of the far-infrared band. The results of this comparison analysis are shown in Fig. 4, where no vacuum was included for any of the models so that the comparison would be as fair as possible. As would be expected, a simple closed waveguide with an absorber filling its cross-secion, and shorted at the closed end of the guide, produces a predictable periodic rise and fall in terms of power absorbed (Fig. 4 (left)). Expanding the closed end of the guide into a cylindrical cavity serves to slightly smooth-out these resonances, but a large amount of variance is still observed across the band. Fig. 4 (right) then shows the predicted improvements for more complex geometries. The hemispherical cavity significantly reduces the depth of the resonant dips, and increases the overall coupling across the band. Clearly, a sinusoidal profile exhibits the best performance across the band, however machining a large-format array of micron-scale cavities with such a complex geometry would be very challenging. As such, the pyramidal cavity was determined to be optimum selection, as it too provides a much-improved increase in coupling and flatness, while also relatively straight-forward to manufacture.

Having settled upon the pyramidal geometry cavity for further analysis, the mode-matching simulation results were then compared with COMSOL FEM simulations for verification. Fig. 5 (left) shows relatively good agreement between the two modelling techniques, considering they are based on completely different theoretical methods. Again, very good predicted coupling of signal to the detector across the frequency band for a 200 μm^2 Ta absorber is shown. The average value across the band is 91.9%, with a standard deviation of 8.7%.

There is a desire to keep the absorber as small as possible since the detector's time constant is directly related to its size. A smaller absorber will therefore result in a faster speed of response. Fig. 5 (right) shows that if the absorber size is reduced to 100 μm^2 there is clearly a reduction in predicted absorber efficiency across the band, but a band average of 81.1% is still considered quite good. There is a significant increase in the level of variance across the band though, with a standard deviation of 15.7%. Fig. 6 (left) shows the predicted band average efficiency values for a range of absorber sizes housed in the double-pyramid cavity structure, where the error bars represent the standard deviation across the band for each absorber size. Both FEM and mode-matching methods were used for the simulations, again showing very good agreement.

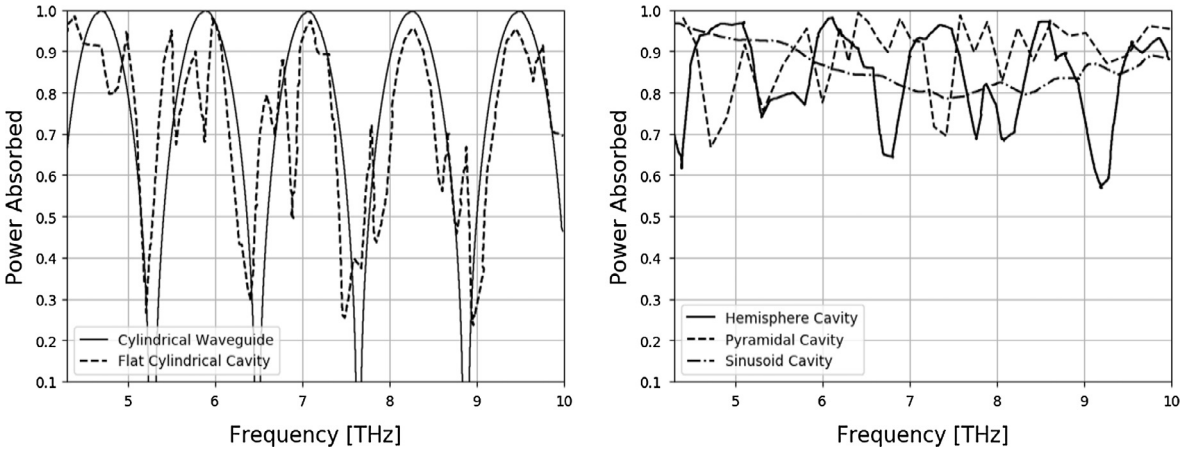

Fig. 4. *Left*: The predicted fraction of signal absorbed by a Ta absorber fulling filling a 200 μm^2 square waveguide, compared to the same 200 μm^2 absorber in the centre of a 400 μm^2 cavity with a flat backshort. *Right*: Comparison of signal absorbed by the same Ta absorber in the centre of hemispherical, pyramidal, and sinusoidal cavities.

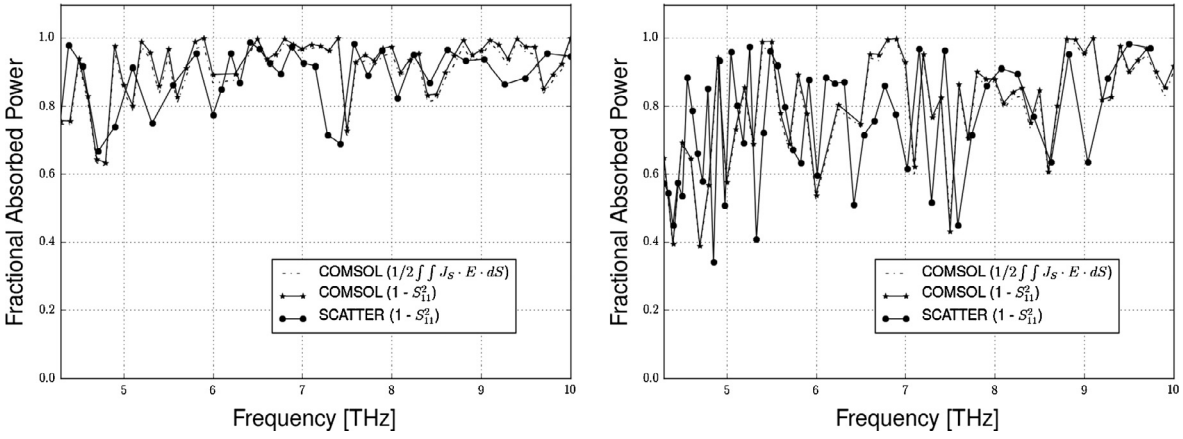

Fig. 5. *Left*: The predicted fraction of signal absorbed by a 200 μm^2 Ta absorber in the new design pyramidal cavity. The results from the mode-matching approach are compared to both the direct and indirect methods of COMSOL. *Right*: Results for the smaller 100 μm^2 absorber.

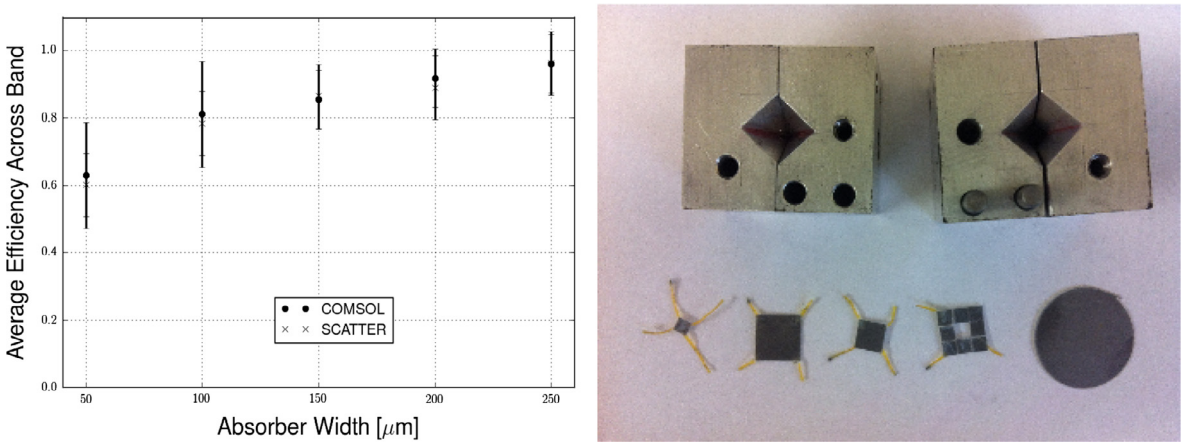

Fig. 6. *Left*: The predicted band-average (4.3–10 THz) signal absorbed by various Ta absorber sizes in the new design pyramidal cavity. The error bars represent the standard deviation in absorption values across the frequency band. *Right*: A photograph of the scaled-up cavity for testing, and scaled-up pieces of Ta absorber material.

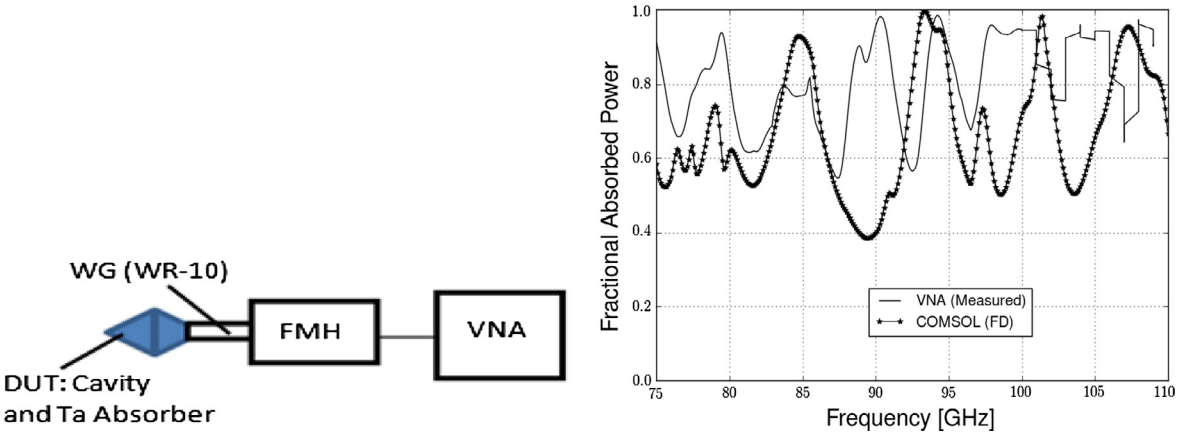

Fig. 7. *Left*: Schematic of the single-head W-band VNA (vector network analyser) setup used for measuring the pyramidal absorbing cavities. FMH is the frequency multiplier head, and WG is the waveguide feed with dimensions of 2.54 × 1.27 mm. *Right*: Results of power absorbed by an 8 × 8 mm Ta absorber in a scaled pyramidal cavity, inferred from the return power of the VNA system. The predicted results from the FEM model are shown also.

While it would be expected that a larger absorber should exhibit overall better coupling, it is not entirely clear why the level of variance across the band is so much affected by absorber size. Looking closely at Fig. 5, there are in fact a small number of frequency values where coupling increases for the smaller absorber, quite significantly at around 4.9 and 7.4 THz ($\lambda = 61.2$ µm and 40.5 µm, respectively). However, for the majority of frequency values the coupling is lower for the smaller absorber. Ultimately, the increased variance is a result of some frequencies being adversely affected more than others by the smaller absorber size. Since the physical size of the smaller absorber's cross-section is comparable to the wavelengths of the signal, the increased variance is likely due to a relationship between the electrical size of the absorber relative to a given wavelength. This effect is somewhat similar to the function of a planar radio receiver or patch antenna. Then, once the absorber is made much larger than the wavelength, this antenna effect is negligible and the absorber behaves as a classical optical detector, with less variance observed. Such effects were analysed in some detail in [25].

4. Experimental verification

4.1. Coherent scaled measurements

In order to verify the computational simulations, a 25.4× scale model was designed and built for testing at W-band frequencies (75–110 GHz). The scaled-up cavity and feed, together with the scaled Ta absorbers are shown in Fig. 6 (right). The 25.4× scale, based on scaling the 100 µm^2 waveguide to the width of the WR-10 waveguide (2.54 mm) translates to a pyramid with a base of 10.16 mm^2. A VNA (vector network analyser) was used in combination with a frequency multiplier head to generate and detect the W-band signals. A schematic of the set-up is shown in Fig. 7 (left). The scale tests were somewhat limited in frequency range. When scaled correctly, the span of frequencies only represents a scaled range of 1.905–2.79 THz. Nonetheless, good agreement between simulation and measurement in this frequency range would give confidence to the validity of the simulations and the approach of modelling the Ta absorber as an infinitely thin resistive sheet.(see Fig. 8)

An 8 × 8 mm squared sapphire substrate of thickness 0.27 ± 0.02 mm, containing an ≈ 7 nm layer of Ta on its surface, was positioned in the centre of the scaled double-pyramid cavity structure. Due to the comparable size of the W-band wavelengths to the substrate thickness, the sapphire material properties were also included in the FEM model. An analysis of return power (S_{11}) was carried out for a frequency sweep across the W-band, in steps of 50 MHz. A frequency domain FEM model of the system was created with COMSOL Multiphysics, which was not too computationally demanding given the relatively low frequencies. As can be seen from Fig. 7 (right) the agreement between simulation and measurement is not very good for the scale model VNA tests, with

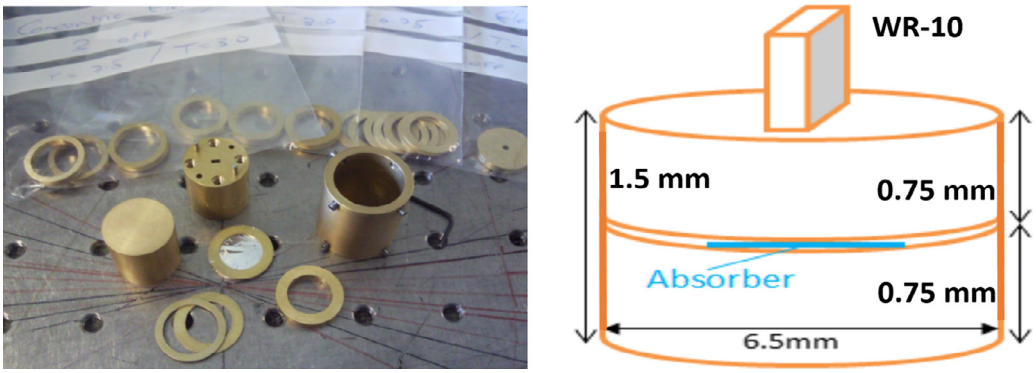

Fig. 8. *Left*: The components of the W-band cylindrical cavity kit that can be used to assemble a large variety of cavities with varying dimensions. *Right*: Illustration of the flat, cylindrical cavity that was assembled for measurement at W-band frequencies, for verification of simulations.

the simulations generally showing a lower level of absorbed power compared to the result deduced from the measurements. The conclusion drawn from this was that the angled walls of the pyramidal cavity cause significant power to be scattered into higher order modes which cannot exit through the single-mode W-band waveguide port. This is not necessarily a bad thing, as there is no reason why these higher-order modes will not also be absorbed by the Ta. However, since the idealised FEM model is purely single-moded, it is not a true representation of the over-moded nature of the pyramidal cavity.

In an effort to carry out a test where measurement and simulation were more representative of one another, namely a better behaved, lower scattering system, a cavity with straight walls and flat backshort were both measured and modelled. A cylindrical cavity of length 1.5 mm was used, with the Ta coated substrate positioned midway in the cavity, with the Ta coated side of the substrate facing the backshort. Fig. 9 (left) shows the return power parameter S_{11} across the W-band, and Fig. 9 (right) shows the power absorbed by the Ta, deduced from the S_{11} data. Clearly there is much better agreement between measurement and simulation in this case, as the mode purity was better constrained in this example. A CST [26] finite-difference time domain (FDTD) model was used as well as the frequency domain (FD) COMSOL [17] model for further verification.

4.2. Higher frequency FTS measurements

To test the scale models at frequencies beyond the range available with the W-band VNA set-up at Maynooth University's labs, a globar source was used in combination with a cryogenic cooled bolometer and an FTS (Fourier transform spectrometer) at a lab at SRON (Netherlands Institute for Space Research), Groningen. The experimental set-up was essentially an FTS reflectometer, in that it was the return power that was analysed in order to deduce the level of signal absorbed by the Ta sheet. Fig. 10 shows a schematic of the set-up.

The globar source was powered with 5 V and a current of 2.65 A. By means of an external Mylar beam splitter of thickness 100 ± 20 μm, approximately half the beam was directed to the cavity via the feed horn, with the other half of the signal lost. Any signal returned from the cavity was directed toward the FTS (again via the beam splitter), and then to the bolometer for detection. An optical chopper, set to a frequency of approximately 30 Hz was used in combination with a lock-in amplifier to minimise the detection of low frequency noise. A low pass filter housed in the cryostat was also used with the bolometer to block frequencies above 3THz. Each of the FTS scans performed (Fig. 11 (left)) had a step-size of 25 μm, giving access to a maximum frequency of 3.33 THz in the Fourier transformed data. The complete length of each scan was 16 mm, yielding a spectral resolution of 4.682 GHz.

In an attempt to measure the stability of, and noise in the complete setup, separate scans were completed one day apart, with all components powered off in the time between scans. Fig. 12 (left) shows the spectra from both days overlaid, while Fig. 12 (right) shows the Day 2 result subtracted from the Day 1 result, revealing a noise level on the order of 0.01 mV. Comparing the noise level to the data on Day 1 or Day 2 indicates an SNR of around 2–10, depending on the frequency.

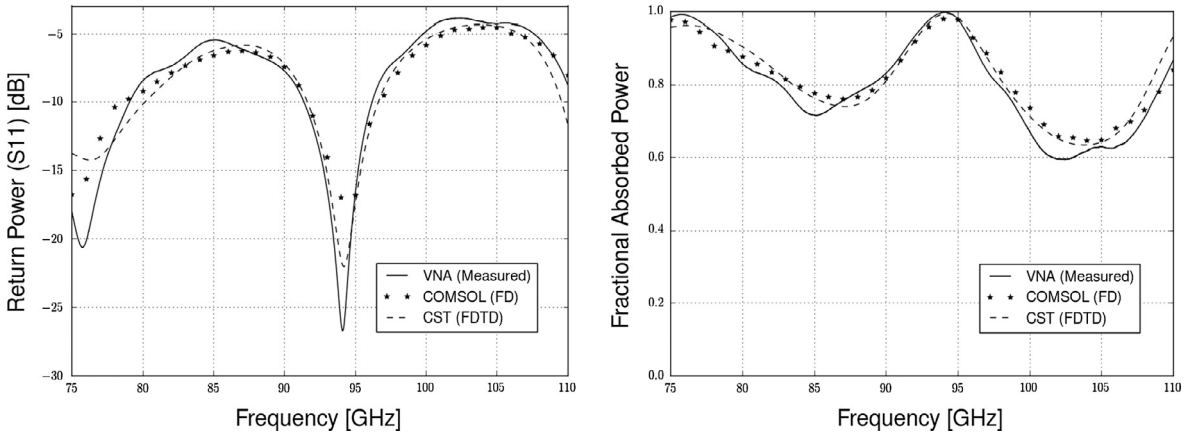

Fig. 9. *Left*: VNA return power (dB) from a cylindrical cavity of radius 6.5 mm and length 1.5 mm, with an 8×8 mm Ta absorber positioned 0.75 mm from the flat backshort. The predicted results from both a FEM model and FIT model are shown also. *Right*: Results of power absorbed by the Ta absorber, inferred from the return power data shown to the left.

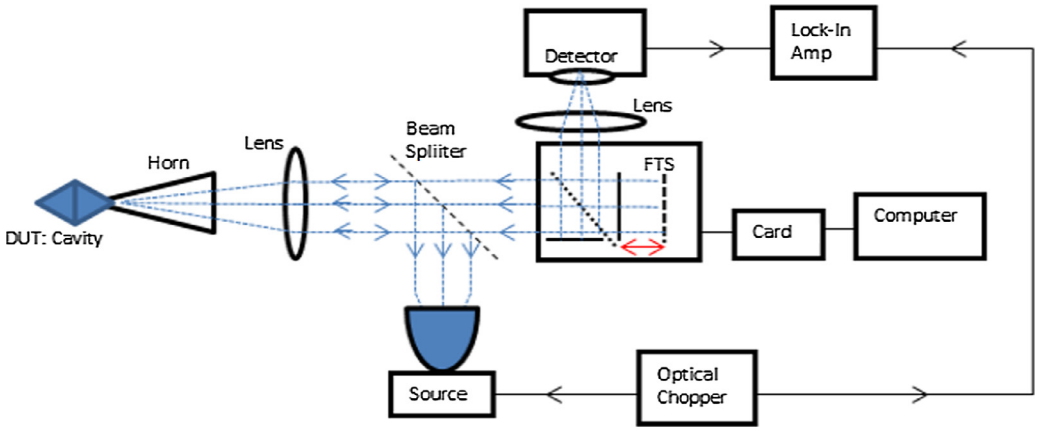

Fig. 10. Schematic of the globar, bolometer, and FTS measurement system used for higher frequency characterisation of the new cavity design.

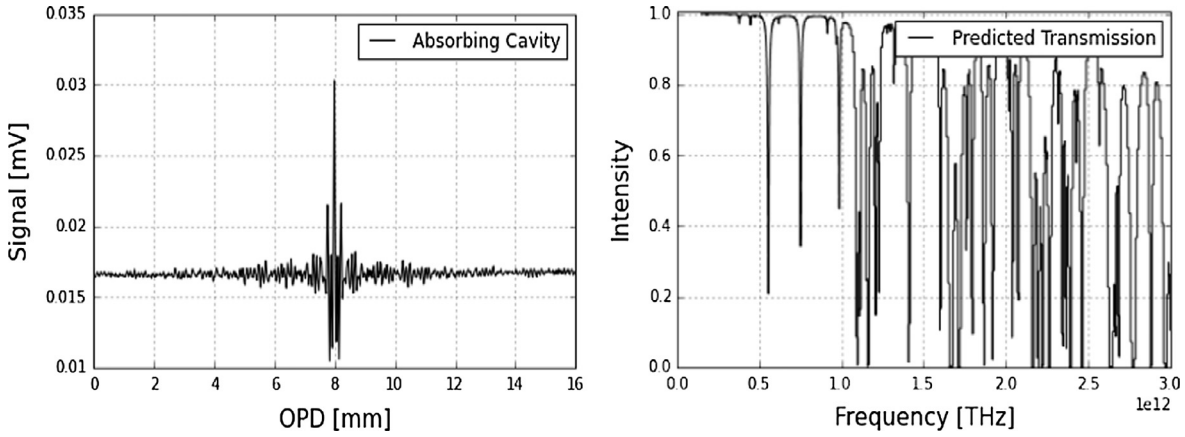

Fig. 11. *Left*: An interferogram recorded using the FTS reflectometer measurement system at SRON. *Right*: Predicted atmospheric transmission for an optical path of 1 m for frequencies up to 3 THz, calculated with an online tool [27].

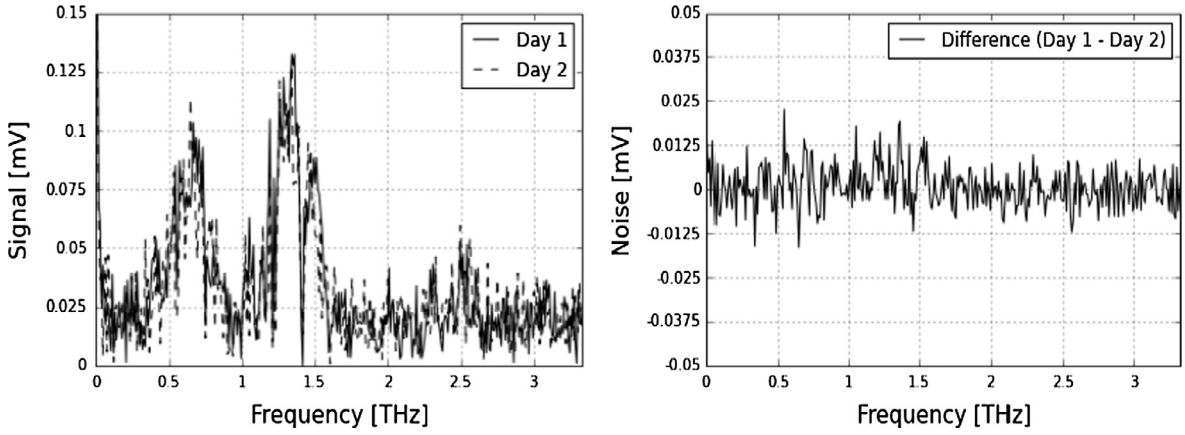

Fig. 12. *Left*: Spectra recorded on two separate days for an 8 × 8 mm Ta absorber in the scaled pyramidal cavity, achieved by Fourier transforming the interferogram data from the FTS reflectometer scans. *Right*: The result of subtracting the spectrum from the Day 1 data from that of the Day 2 data. This gives an approximate measure of the noise in the system.

It was assumed that the best way to account for, and remove, all spectral features intrinsic in the system itself (and not due to the absorbing cavity) was to carry out two sets of FTS measurements; one with the absorbing cavity connected to the horn/waveguide, and one with the cavity replaced by a mirror at the waveguide entrance. Fig. 13 (left) shows the two resulting spectra. There is clearly a noticeable decrease in returned power when the absorber and cavity are in place, indicating a measurable response of the absorbing cavity. Fig. 13 (right) shows the result of subtracting the absorbing cavity signal from the mirrored horn/waveguide signal. The predicted efficiency of a 100 μm beamsplitter, based on theoretical work reported by [28] is overlaid on the data. Thus, the large null in the data at frequencies around 0.95 THz is not surprising. Fig. 14, then, shows the result of dividing the mirrored

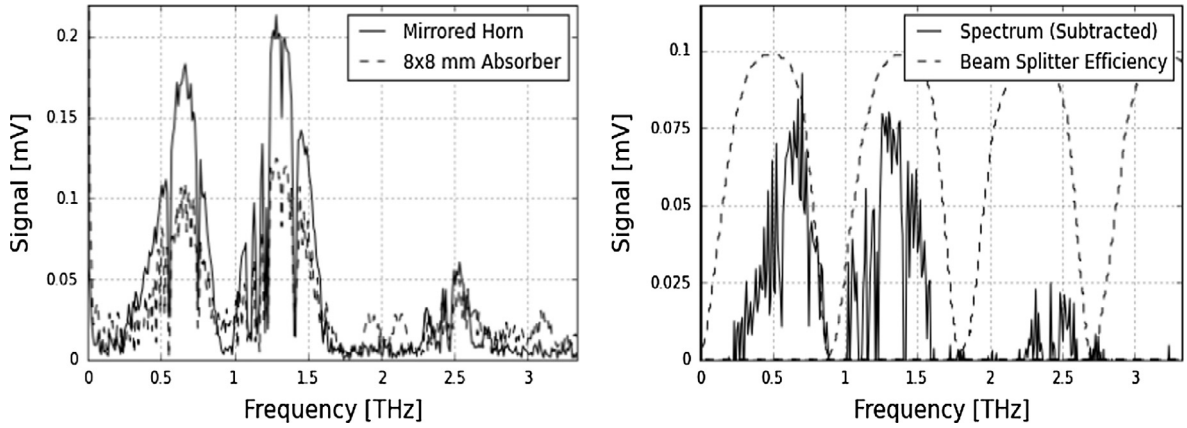

Fig. 13. *Left*: The spectra corresponding to an 8 × 8 mm Ta absorber in a scaled pyramidal cavity, and the case where the absorber and cavity were replaced be a mirror. *Right*: The result of subtracting the absorbing cavity data from the mirrored waveguide data.

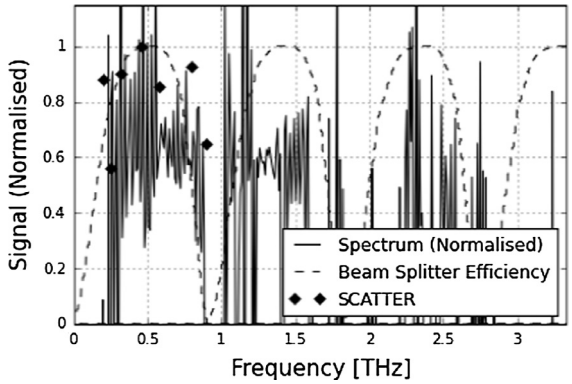

Fig. 14. The result of subtracting the absorbing cavity data from the mirrored waveguide data, and then dividing the result by the mirrored waveguide data for normalisation.

horn/wavguide data into the previous result in an attempt to normalise the data, where again the beam splitter efficiency is overlaid on the plot. Predicted results calculated using the mode-matching method with SCATTER are also shown in Fig. 14, where relatively good agreement is shown for frequencies that were possible to simulate (up to 0.9 THz). A PC with 16 Giga Bytes of RAM exhausted its memory for the FEM approach for frequencies beyond 0.2 THz, therefore no FEM results are shown in Fig. 14.

It is difficult to extract a precise spectral response of the absorbing cavity with the reflectometer setup. As can be seen in the normalised data in Fig. 14, some of the values are above unity which should not be the case for normalised data. This is obviously a result of dividing the measured signal by very small values which resulted from noisy data points. Furthermore, there is very little usable signal at frequencies above 1.6 THz. This is likely due to atmospheric absorption since the predicted transmission begins to fall off for the higher frequencies, as shown in Fig. 11 (right). For a more accurate characterisation of this new cavity design future work will be required, where a direct readout of absorbed signal by the Ta can be achieved (rather than the current indirect approach). Progress is currently being made in terms of securing funding for this next phase of work.

5. Conclusion

In an attempt to increase coupling of signal to far-infrared TES detector absorbers, and to increase uniformity of frequency response of the TES's, a new cavity backshort was designed. The new design is based on a silicon crystal etching manufacturing technique, which results in a natural pyramidal geometry with a surface finish significantly smoother than can typically be achieved by machining. The performance of the new cavity design was modelled using the commercially available COMSOL Multiphysics package, and with a customised mode-matching code for improved computational efficiency. The two modelling techniques were shown to be in good agreement, both showing the new cavity design to have excellent performance across the 4.3–10 THz frequency band.

In an effort to verify the theoretical results, a scale model (25.4x) was built for testing at W-band frequencies with a single-port VNA system and frequency multiplier head. Due to significant disagreement between model and measurement for the pyramidal scale model, a flat cylindrical cavity format was also tested. The cylindrical cavity geometry was designed to limit the level of power scattering to higher-order modes, and it resulted in much better agreement between measurement and simulation, thereby giving confidence as to the validity of the simulations.

Given the limitations in the range of frequencies accessible with the VNA system, a second measurement campaign was carried out using a globar source and a highly sensitive cryo-cooled bolometer. An FTS was used in a reflectometer format to measure the spectral response of the Ta absorber housed in the new cavity design at frequencies up to 3.3 THz. The FTS system resulted in a measurable signal at most frequencies within the passbands of the 100 μm beam splitter, however it was difficult to have complete confidence in the results across the full measured frequency range due to atmospheric absorption at the higher frequencies, and nulls in the data due to beam splitter efficiency.

Future work will be required for a more accurate characterisation of the new cavity design at the highest frequencies of the far-infrared band. The future work should be based on a real-size cavity for testing, and a direct read-out of absorbed power should be implemented.

Conflict of Interest

The authors declared that there is no conflict of interest.

Acknowledgment

The authors would like to acknowledge support from the ESA Technical Research Programme (TRP) entitled "New Technology High Efficiency Horn Antennas for Cosmic Microwave Background Experiments and Far-Infrared Astronomy", ESA contract No. - RFQ

3-6418/11/NL/Cbi. The corresponding author also acknowledges financial support from Science Foundation Ireland. This publication has emanated from research supported in part by a Grant from Science Foundation Ireland under Grant No. 15/IA/2880.

Appendix A. Supplementary material

Supplementary data associated with this article can be found, in the online version, at https://doi.org/10.1016/j.infrared.2018.01.004.

References

[1] S. Itsuki, K. Hidehiro, O. Shinki, I. Daisuke, W. Takehiko, F. Naofumi, Sensitivity estimates for the spica mid-infrared instrument (smi), in: Proc. SPIE 9904, Space Telescopes and Instrumentation 2016: Optical, Infrared, and Millimeter Wave 99043V, 2016, 12p. doi:https://doi.org/10.1117/12.2232402. <http://spie.org/Publications/Proceedings/Paper/10.1117/12.2232402>.

[2] C. Pastor, et. al., Safari optical system architecture and design concept, in: Proc. SPIE 9904, Space Telescopes and Instrumentation 2016: Optical, Infrared, and Millimeter Wave 99043U, 2016, 12p. doi:https://doi.org/10.1117/12.2232786. <http://spie.org/Publications/Proceedings/Paper/10.1117/12.2232786>.

[3] M. Servillat, A. Coleiro, S. Chaty, F. Rahoui, J. Zurita-Heras, Herschel observations of dust around the high-mass X-ray binary gx 301-2, Astrophys. J. 797 (2) (2014) 10, https://doi.org/10.1088/0004-637X/797/2/114, id. 114.

[4] I. Oteo, Dust correction factors over 0<z<3 in massive star-forming galaxies derived from a stacking analysis of herschel data, Astron. Astrophys. 572 (2014) 12, https://doi.org/10.1051/0004-6361/201424607, id. L4.

[5] M. Werner, G. Fazio, G. Rieke, T. Roellig, D. Watson, First fruits of the spitzer space telescope: galactic and solar system studies, Ann. Rev. Astron. Astrophys. 44 (1) (2006) 269–321.

[6] M. Audley, G. de Lange, J.-R. Gao, P. Khosropanah, R. Hijmering, M. Ridder, P.D. Mauskopf, D. Morozov, N.A. Trappe, S. Doherty, Optical performance of an ultra-sensitive horn-coupled transition-edge-sensor bolometer with hemispherical backshort in the far infrared, Rev. Sci. Instrum. 87 (4). doi: https://doi.org/10.1063/1.4945302. <http://arxiv.org/abs/1603.07944>.

[7] C. Bracken, Electromagnetic techniques for analysis and design of ultra sensitive receivers for far-infrared astronomy [Ph.D. thesis], National University of Ireland, Maynooth (Maynooth University), 2015.

[8] M. Audley, G. de Lange, C. Bracken, Detector and calibration-source models for the safari detector test facility, in: COMSOL Conference Proceedings WTC Rotterdam, the Netherlands. <http://www.comsol.de/paper/download/182113/audleyabstract.pdf>.

[9] M. Trupke, F. Ramirez-Martinez, E.A. Curtis, J.P. Ashmore, S. Eriksson, E.A. Hinds, Z. Moktadir, C. Gollasch, M. Kraft, G. Vijaya Prakashb, J.J. Baumberg, Pyramidal micromirrors for microsystems and atom chips, Appl. Phys. Lett. 88 (7) (2006) 071116-1–071116–3, https://doi.org/10.1063/1.2172412.

[10] S. Pollock, Integration of magneto optical traps in atom chips [Ph.D. thesis], Centre for Cold Matter, Department of Physics, Imperial College London, 2010.

[11] G.N. Lewis, Z. Moktadir, C. Gollasch, M. Kraft, S. Pollock, F. Ramirez-Martinez, J. P. Ashmore, A. Laliotis, M. Trupke, E.A. Hinds, Fabrication of magnetooptical atom traps on a chip, J. Microelectromech. Syst. 18 (2) (2009) 347–353, https://doi.org/10.1109/JMEMS.2008.2007200. <http://ieeexplore.ieee.org/stamp/stamp.jsp?arnumber=4797887&tag=1> .

[12] M.D. Audley, G. de Lange, M. Ranjan, J.-R. Gao, P. Khosropanah, M.L. Ridder, P.D. Mauskopf, D. Morozov, S. Doherty, N. Trappe, S. Withington, Measurements of the optical performance of prototype tes bolometers for safari, J. Low Temp. Phys. 176 (5) (2014) 755–760, https://doi.org/10.1007/s10909-013-0984-5.

[13] K. King, S. Leeks, SPIRE Instrument User Manual, 2009. <www.cst.com>.

[14] M. ELLIS, Scuba-2 ccd-style imaging for the jcmt, Exp. Astron. 19 (2005) 169–174, https://doi.org/10.1007/s10686-005-9008-z. <https://link.springer.com/article/10.1007/s10686-005-9008-z> .

[15] T. Baum, D.J. Schiffrin, AFM study of surface finish improvement by ultrasound in the anisotropic etching of Si in KOH for micromachining applications, J. Micromech. Microeng. 7 (4) (1997) 338. <http://stacks.iop.org/0960-1317/7/i=4/a=010> .

[16] J. Park, S. Jeong, H. Lee, H. Jeong, E. suk Lee, A study on the chemical mechanical micro-machining (C3M) process and its application, J. Mater. Process. Technol. 130131 (2002) 390–395, https://doi.org/10.1016/S0924-0136(02)00732-X, {AFDM} 2002 S.I. <http://www.sciencedirect.com/science/article/pii/S092401360200732X> .

[17] COMSOL, AB, COMSOL v. 5.2, Stockholm, Sweden, 2016.

[18] S. Withington, C. Thomas, D. Goldie, Partially coherent optical modelling of the ultra-low-noise far-infrared imaging arrays on the spica mission, available from: <arXiv:1307.7278> [astro-ph.IM]. <http://arxiv.org/pdf/1307.7278v1.pdf>.

[19] S. Doherty, Optical and quasi-optical design and analysis of astronomical instrumentation including a prototype safari pixel [Ph.D. thesis], National University of Ireland, Maynooth (Maynooth University), 2012.

[20] G. Chattopadhyay, J. Glenn, J. Bock, B. Rownd, M. Caldwell, M. Griffin, Feed horn coupled bolometer arrays for spire: design, simulations, and measurements, IEEE Trans. Microw. Theory Tech. 51 (10) (2003) 2139–2146, https://doi.org/10.1109/TMTT.2003.817428. <http://adsabs.harvard.edu/abs/2003ITMTT..51.2139C> .

[21] C. Bracken, on behalf of the FP7-FISICA Consortium, Optical and quasi-optical analysis of system components for a far-infrared space interferometer, Proceedings of SPIE 9362 Terahertz, RF, Millimeter, and Submillimeter-Wave Technology and Applications VIII (93620N), 2015, 12p. doi:https://doi.org/10.1117/12.2076385.

[22] E. Gleeson, Single and multi-mode corrugated horn design for cosmic microwave background experiments [Ph.D. thesis], National University of Ireland, Maynooth (Maynooth University), 2004.

[23] N. Trappe, C. Bracken, S. Doherty, J. Gao, D. Glowacka, D. Goldie, M. Griffin, R. Hijmering, B. Jackson, P. Khosropanah, P. Mauskopf, D. Morozov, A. Murphy, C. O'Sullivan, M. Ridder, S. Withington, Optical modeling of waveguide coupled TES detectors towards the safari instrument for spica, Proc. SPIE 8452 (VI) (2012) 84520L-84520L-6. doi:https://doi.org/10.1117/12.926760.

[24] J.A. Murphy, S. Doherty, N. Trappe, C. Bracken, T. Peacocke, C. O'Sullivan, New developments in waveguide mode-matching techniques for far- infrared astronomy, Proc. SPIE 8261 (2012) 82610F–82610F–7. doi:https://doi.org/10.1117/12.908068.

[25] C. Thomas, S. Withington, D. Chuss, E. Wollack, S. Moseley, Modeling the intensity and polarization response of planar bolometric detectors, J. Opt. Soc. Am. A Opt. Image Sci. Vision 27 (5) (2010) 1219–1231, https://doi.org/10.1364/JOSAA.27.001219. <https://www.osapublishing.org/josaa/abstract.cfm?uri=josaa-27-5-1219> .

[26] CST Microwave Studio, 2016. <www.cst.com>.

[27] SpectralCalc, <http://www.spectralcalc.com/info/about.php,accessed:05June 2016>.

[28] D. James, J. Ring, The efficiency of beamsplitters in the far infra-red michelson interferometer, Journal de Physique Colloques 28 (C2) (1967), https://doi.org/10.1051/jphyscol:1967227, C2-150-C2-152 <https://hal.inria.fr/jpa-00213205/document> .